

# Impact of the Capacitance of the Dielectric on the Contact Resistance of Organic Thin-Film Transistors

K. Zojer,<sup>1,\*</sup> E. Zojer,<sup>1</sup> A. F. Fernandez,<sup>1</sup> and M. Gruber<sup>2</sup>

<sup>1</sup>*Institute of Solid State Physics, NAWI Graz, Graz University of Technology, Petersgasse 16, 8010 Graz, Austria*

<sup>2</sup>*Institute of Theoretical and Computational Physics, NAWI Graz, Graz University of Technology, Petersgasse 16, 8010 Graz, Austria*

(Received 1 June 2015; revised manuscript received 22 August 2015; published 8 October 2015)

As the operation of organic thin-film transistors relies exclusively on injected charge carriers, the gate-induced field assumes a dual role: It is responsible for charge-carrier accumulation and, provided that an injection barrier at the contact-semiconductor interface is present, aids charge-carrier injection across this barrier. Besides the gate-source bias, the thickness of the insulator and its dielectric constant influence the gate field. Here, we explore the impact of the capacitance of the gate dielectric on the performance of organic thin-film transistors utilizing drift-diffusion-based simulations comprising a self-consistent consideration of injection. Upon varying the capacitance of the insulating layer, we observe a conceptually different behavior for top-contact and bottom-contact architectures. Top-contact devices possess a nearly constant contact voltage in the linear regime leading to an apparent mobility lowering. In strong contrast, bottom-contact architectures possess non-Ohmic contact resistances in the linear regime due to a contact voltage whose value depends strongly on both the gate-source bias and the capacitance. Counterintuitively, this is accompanied by a mobility being apparently unaffected by the substantial contact resistance. Additionally, threshold-voltage shifts appear due to gate-limited injection. The latter is particularly dominant in bottom-contact architectures, where the threshold voltages steeply increase with the thickness of the insulating layer.

DOI: [10.1103/PhysRevApplied.4.044002](https://doi.org/10.1103/PhysRevApplied.4.044002)

## I. INTRODUCTION

Organic thin-film transistors (OTFTs) hold the promise of realizing flexible, even transparent electronic circuits at low cost. In terms of switching speed, they are promising candidates for applications in radio-frequency identification (RFID) tags and in active-matrix organic light-emitting displays [1]. However, a successful introduction of OTFT-based electronics on the market requires a reliable operation at frequencies in the megahertz region [2]. Such an additional boost in switching speed can be expected from enhancing the drain-source conductance. As originally inspired by the widely used gradual channel approximation (GCA), one seeks to enlarge the drain-source current by either (i) reducing channel lengths [3–5], (ii) reducing the insulator thicknesses (geometry parameters) [6–8], (iii) profoundly increasing charge-carrier mobilities [9–11], or (iv) increasing the dielectric constant of the insulating material  $\epsilon_{r,\text{ins}}$  (material parameters) [1,12–15]. A complication in this context is that highly promising advances in reaching this goal demonstrate that the contact resistance  $R_C$ , known to reduce the current, becomes particularly prominent when approaching the limits of the

aforementioned scaling parameters, such as submicrometer channel lengths and mobilities exceeding  $1 \text{ cm}^2/(\text{V s})$  [1,4,16,17]. Previous numerical studies indicated that (i)  $R_C$  occurs in part due to the presence of an injection barrier and that (ii) the related voltage losses at the contact strongly depend on the device architecture due to the geometry-specific distribution of the electric field [18–20].

In general, injection plays a much more crucial role for organic transistors compared to transistors consisting of conventional inorganic semiconductors (e.g., MOSFETs). Owing to their large band gap, organic semiconductors (OSC) possess only a negligible density of mobile charges at room temperature. Moreover, the materials are usually not electrically doped. For the time being, contemporary attempts to utilize doping in OTFTs are, in essence, aimed at establishing efficient injection of the carriers with the desired charge polarity without interference from the level alignment at the immediate metal-semiconductor interface. I.e., they typically aim at realizing Ohmic contacts [16,21]. Thus, the OTFT operation cannot rely on  $pn$  junctions, i.e., on the control of the associated space-charge region. As a consequence, OTFTs operate in accumulation rather than depletion or inversion (apart from a recently reported attempt [21]). In doing so, they exclusively rely on charges injected at the contacts. This is further illustrated by the fact that organic CMOS devices do not consist of transistors

\*Corresponding author.  
karin.zojer@tugraz.at

with different doping profiles. Rather, the CMOS concept is realized by a combination of transistors with deliberately chosen semiconductor-electrode properties such that the contacts in one OTFT predominantly inject electrons while in a second one holes are injected.

It is, therefore, crucial to explore and comprehend how the material and geometry parameters in the focus of scaling efforts affect injection in the first place. In this work, we explore how changing the insulator capacitance alters the operation of OTFTs due to imperfect injection as, in analogy to the gate bias  $V_{GS}$ , it does not only determine the carrier density in the channel but also directly modifies the electric-field distribution and, thus, the current being injected at the contact. To that aim, we employ drift-diffusion-based simulations for two different device architectures, i.e., the staggered (top-contact bottom gate) and the coplanar (bottom-contact bottom gate) one, in which the thickness and the dielectric constant of the insulator are varied. As we expect an intricate interplay of injection and transport through the transistor channel, we will also determine how the observed effects depend on the present material properties, i.e., on the charge-carrier mobility and the injection barrier.

## II. METHODOLOGY

To study the impact of the gate insulator capacitance, the gate bias, and the device architecture on injection, we performed drift-diffusion-based simulations on a two-dimensional cross section of the transistors, as schematically indicated in Fig. 1.

The details of our implementation are described in considerable detail in Refs. [18,22] and, in particular, in the Supplemental Material of Ref. [18] (available free of charge from the publisher's home page). In essence, we

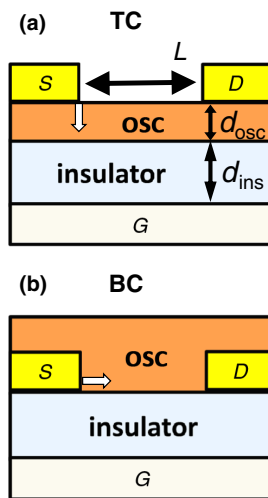


FIG. 1. Schematic cross section of TC (a) and BC OTFTs (b). The white arrows indicate the position and direction from which injection mainly occurs.

solve the current density and continuity equation for holes and the Poisson equation self-consistently on a two-dimensional nonuniform rectangular grid. The net carrier injection at the contacts is self-consistently determined for any given point of operation by obtaining the contributions of thermionic emission, tunneling, and interface recombination resulting from the field- and carrier-density distribution present at the contacts [18]. For varying the capacitance per unit area we either alter the thickness  $d_{ins}$  or the dielectric constant  $\epsilon_{r,ins}$ . We successively refine the mesh used for the discretization of the cross section, until both the current as well as the charge-carrier density are not affected by the chosen discretization any more. The  $I$ - $V$  curves are obtained for hole-conducting–top-contact–bottom-gate (TC) and bottom-contact–bottom-gate (BC) devices with  $L = 5 \mu\text{m}$ ,  $W = 7 \text{ nm}$ , and  $\epsilon_{r,OSC} = 3.4$  (matching the range of values reported for pentacene [23]). We choose  $\text{SiO}_2$  with  $\epsilon_{r,ins} = 3.9$  as our reference dielectric medium considering that it plays exactly this role in organic electronics. Furthermore, we consider  $\epsilon_{r,ins}$  values of 11.7 and 35.1 obtained by consecutively tripling  $\epsilon_{r,\text{SiO}_2}$ . The thickness of the organic semiconducting (OSC) layer in the top-contact–bottom-gate device is set to  $d_{OSC} = 30 \text{ nm}$ . This value is also chosen for the height of the source and drain contacts in the BC OTFTs [Figs. 1(a) and 1(b)]. The total thickness of the semiconductor layer in the BC OTFT is  $d_{OSC} = 40 \text{ nm}$ . We set the temperature to  $T = 300 \text{ K}$ , and the density of states in the active material close to the contacts entering into the interface recombination current to  $3 \times 10^{27} \text{ m}^{-3}$  [24]. The threshold voltage entering the simulations,  $V_{th}^0$ , is defined as the flatband voltage in the spirit of Meijer *et al.* [25]. Here, it is exactly zero as we assume identical electrode materials and do not consider trapped interface charges. For the operating conditions, if not stated otherwise, we choose  $V_{DS} = -20 \text{ V}$  for the transfer characteristics and  $V_{GS}$  either  $-10$  or  $-35 \text{ V}$  for the output characteristics. The charge-carrier mobility  $\mu$  is set to a constant value of  $1 \text{ cm}^2/(\text{V s})$  and the nominal injection barrier  $\Phi$  (defined as the offset between the chemical potential in the metal and the transport level in the semiconductor) is either  $0.0$  or  $0.5 \text{ eV}$  [26]. To corroborate our findings, additional calculations with mobilities of  $\mu = 0.1 \text{ cm}^2/(\text{V s})$  and  $\mu = 10 \text{ cm}^2/(\text{V s})$  as well as with an intermediate injection barrier of  $\Phi = 0.3 \text{ eV}$  are performed. For each point of operation, the contact voltages are determined using the procedure outlined in Ref. [18]. The basic idea is to determine first the evolution of the potential in the channel region from the simulated potential distributions. The channel potential is then extrapolated to the edges of the contacts; finally, the contact voltage is taken as the difference between this “extrapolated channel potential” and the potential of the source contact. The potential distributions associated with the initial state are determined by solving the Poisson equation within the cross section with the

potentials at the electrodes fixed corresponding to the values of the external biases. The charge density in the insulator is set exactly to zero, while in the semiconductor, a small, homogeneous density of fixed charges of  $10^{10} \text{ m}^{-3}$ , is used as an initial condition to stabilize the self-consistent solution of the Poisson equation [27].

### III. ROLE OF INJECTION FOR THE TRANSISTOR OPERATION

To connect injection to the appearance of a contact resistance, it is useful to recall the following. In the ideal case of homogeneous organic semiconductor layers, the contact resistance can be viewed as arising from two factors: The need to (i) overcome an injection barrier at the contact and (ii) pass through a low conductivity zone prior to reaching the channel entrance [18,28,29]. The former contribution to  $R_C$  arises from the fact that injection occurs across a barrier at the metal-semiconductor interface. The injected current increases markedly if a local electric field present at the contact reshapes the potential barrier and so effectively lowers the barrier height [30]. This local field predominantly originates from the applied gate-source bias and contains further contributions from already injected charges (screening) and from the drain-source bias. The latter contribution is, however, comparably small to the typically large channel-length-to-dielectric-thickness aspect ratio.

Top-contact-bottom-gate OTFTs [Fig. 1(a)] feature a depleted, low-conductivity region between the source contact and the channel entrance. Charge carriers injected at the electrode-semiconductor interface need to travel across this region to reach the dielectric-semiconductor interface, where the channel is formed. In the absence of an injection barrier, this “access region” gives rise to an “access” resistance. However, the presence of an injection barrier adds an additional contribution to the voltage drop across this depletion region due to the need to provide an injection-aiding field at the contact. This renders the contact resistance non-Ohmic. Somewhat counterintuitively, nonzero injection barriers in BC devices [Fig. 1(b)] also lead to the occurrence of a region largely depleted of mobile carriers in the vicinity of the contact. This results in a “depletion” region between the contact and the entrance of the actually conductive channel, even though the injecting facet is located directly at the semiconductor-insulator interface [18,19,23]. Again, there is a contact voltage  $V_C$  dropping across this depletion region that gives rise to a non-Ohmic contact resistance  $V_C/I_{\text{DS}}$ .

In both OTFT architectures, the need to inject across a barrier requires the contact voltage  $V_C$  to adjust such that the admitted injection current matches the space-charge-limited current through the channel. The latter is driven by  $V_{\text{DS}} - V_C$ , i.e., the applied drain-source voltage minus the potential drop due to the contact resistance [18]. As a consequence of this current matching condition, the contact

resistance  $R_C$  and the channel resistance  $R_{\text{ch}}$  act as a non-Ohmic voltage splitter sharing the same current  $I_{\text{DS}}$  [29]. Since the strength of the barrier-shaping field and the extension of the depletion zone depend strongly on the orientation and position of the injecting electrode with respect to the gate electrode, the value of  $R_C$  is determined by factors such as (i) the device architecture, (ii) the charge-carrier mobility, (iii) the injection barrier at the contact, (iv) the point of operation, and (v) geometry parameters such as channel length and thickness of the dielectric layer [18,19,22].

### IV. TRANSISTOR CHARACTERISTICS

To be able to identify the particular impact of injection on the transistor behavior, it is advisable to compare the  $I$ - $V$  characteristics affected by injection to those corresponding to the ideal situation without injection. The commonly used results from the gradual channel approximation (GCA) serve as a starting point for the following discussion. It is known to provide a good description of device characteristics in the absence of a contact resistance (at least as long as the mobility is constant and spatially uniform). The GCA expression yields the current  $I_{\text{DS}}$  [31],

$$I_{\text{DS}} = \frac{W}{L} \frac{\epsilon_0 \epsilon_{r,\text{ins}}}{d_{\text{ins}}} \mu \left( V_{\text{GS}} - V_{\text{th}}^0 - \frac{V_{\text{DS}}}{2} \right) V_{\text{DS}} \quad (1)$$

for  $|V_{\text{GS}}| \gg |V_{\text{DS}}|$  (linear regime), and

$$I_{\text{DS}} = \frac{W}{2L} \frac{\epsilon_0 \epsilon_{r,\text{ins}}}{d_{\text{ins}}} \mu (V_{\text{GS}} - V_{\text{th}}^0)^2 \quad (2)$$

for  $|V_{\text{GS}}| \leq |V_{\text{DS}}|$  (saturation regime). According to Eqs. (1) and (2),  $I_{\text{DS}}$  depends on the externally applied biases  $V_{\text{DS}}$  and  $V_{\text{GS}}$ , on material parameters like the relative dielectric constant of the insulator  $\epsilon_{r,\text{ins}}$  and the charge carrier mobility  $\mu$ , and geometric parameters like the thickness of the insulator  $d_{\text{ins}}$ , and the length  $L$  and width  $W$  of the channel.  $V_{\text{th}}^0$  denotes the threshold voltage and  $\epsilon_0$  the vacuum permittivity. Dividing  $I_{\text{DS}}$  by the capacitance per unit area  $C'$ , which is given by  $C' = \epsilon_0 \epsilon_{r,\text{ins}} / d_{\text{ins}}$ , yields a renormalized current  $i_{\text{DS}}$ . The advantage of using that quantity is that in case the GCA is applicable it is independent of  $C'$  [cf. Eqs. (1) and (2)]. The relation between  $i_{\text{DS}}$ ,  $I_{\text{DS}}$ , the thickness of the insulator, and its dielectric constant is given by

$$i_{\text{DS}} = \frac{I_{\text{DS}}}{C'} = I_{\text{DS}} \frac{d_{\text{ins}}}{\epsilon_0 \epsilon_{r,\text{ins}}}. \quad (3)$$

With this definition any set of  $i_{\text{DS}} - V$  curves (i.e., scaled device characteristics) in an ideal device described by the GCA collapses onto a single curve when the insulator thickness or the dielectric constant are varied. Consequently, deviations from such GCA-based scaled

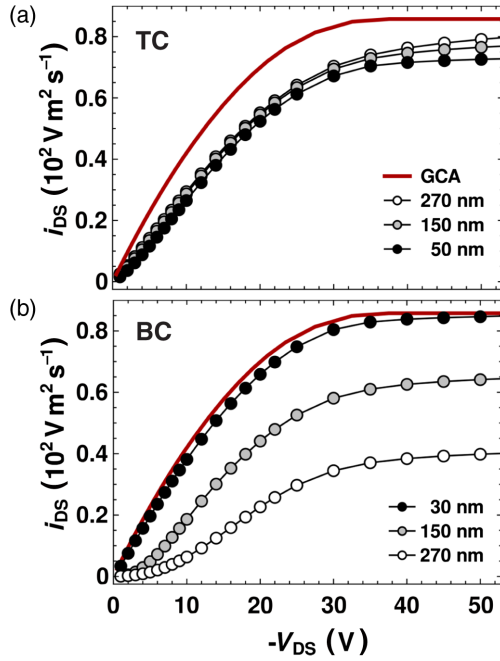


FIG. 2. (a),(b) Scaled output curves  $i_{DS}(V_{DS})$  for an injection barrier  $\Phi = 0.5$  eV for different insulator thicknesses and  $\epsilon_{r,ins} = 3.9$  for a TC (a) and a BC (b) OTFT. For comparison, the result of the gradual channel approximation (red, solid line) is shown. The devices with a mobility  $\mu = 1$  cm<sup>2</sup>/(Vs) and  $L = 5$   $\mu$ m are operated at  $V_{GS} = -35$  V.

characteristics indicate a deviation from an ideal device behavior.

This is shown in Fig. 2 for the BC and TC devices described in Sec. II: The ideal, scaled GCA output curve is

displayed as a thick solid line. In passing, we note that the GCA curve essentially coincides with the results of a drift-diffusion simulation at  $\Phi = 0.0$  eV. The results for an injection barrier of 0.5 eV, however, show marked deviations from the idealized case. Interestingly, these deviations are qualitatively different for the two device architectures. The scaled current in the TC device [Fig. 2(a)] is reduced with respect to the ideal curve by a roughly constant multiplicative factor and is hardly affected by the insulator thickness [Fig. 2(b)]. In strong contrast, the BC devices [Fig. 2(b)] exhibit a pronounced dependence of  $i_{DS}$  on  $d_{ins}$ . While a thin insulator film ( $d_{ins} = 30$  nm) almost reproduces the ideal output curve in spite of the appreciable injection barrier, an increase in  $d_{ins}$  reduces the current (in the saturation regime by a factor of nearly 2 when increasing  $d_{ins}$  to 270 nm). With increasing insulator thickness, the straight rise in the linear regime is also increasingly superseded by an S-shaped curve. Such a nonlinear increase is usually attributed to the occurrence of a contact resistance [32]. In passing, we note that, particularly for the small injection barrier, the S shape observed in the output characteristic can be also caused by (i) the field dependence of the mobility [33] or (ii) the parasitic charging of the regions below the contacts in TC architectures, particularly at small gate and drain-source biases [34].

To explain the apparently architecture-specific behavior, we turn to the scaled transfer characteristics  $I_{DS}(V_{GS})$  for TC and BC devices, as they allow a more in-depth analysis of the role of the injection-aiding gate field that is determined by an interplay between  $V_{GS}$  and  $d_{ins}$ . They are shown in Figs. 3(a) and 3(b). Without an injection barrier  $\Phi = 0$ , the scaled current [blue-filled and open

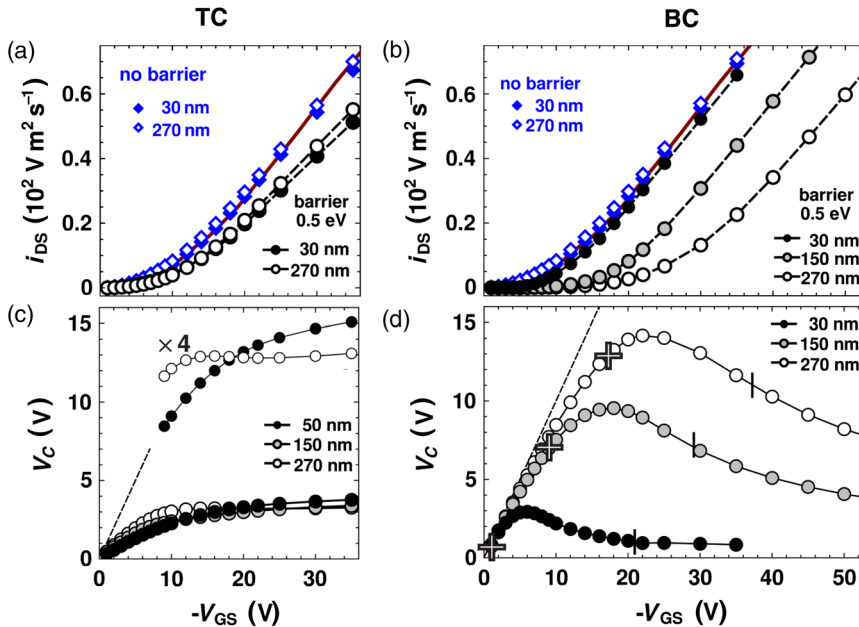


FIG. 3. (a),(b) Scaled transfer curves  $i_{DS}(V_{GS})$  for TC (a) and BC OTFTs (b) for injection barriers of 0 ( $d_{ins} = 30$  nm, filled diamonds;  $d_{ins} = 270$  nm, open diamonds) and 0.5 eV ( $d_{ins} = 30$  nm, filled, black circles; 150 nm, gray circles; and 270 nm, open circles). For comparison, also the curve obtained from applying the gradual channel approximation is shown (solid line). (c) Contact voltage  $V_C$  in TC OTFTs as a function of gate-source bias  $V_{GS}$  for insulator thicknesses of 50 (black circles), 150 (gray circles), and 270 nm (open circles). Also shown are  $V_C$  curves for 50 and 270 nm scaled by a factor of 4. The dashed lines indicate the upper limit of  $V_C$  given by  $V_C = |V_{GS}|$  (for details, see text). (d) Analogous to (c) for BC devices for  $d_{ins} = 30$  (filled circles), 150 (gray circles), and 270 nm (open circles). The crosses and vertical bars indicate  $|V_{GS}| = V_{th}$  and  $|V_{GS}| = |V_{DS}| + V_{th}$  at different  $d_{ins}$ . The devices are operated at  $V_{DS} = -20$  V.

diamonds in Figs. 3(a) and 3(b)] again corresponds excellently to the GCA prediction (red solid line).

Upon increasing the injection barrier to  $\Phi = 0.5$  eV the TC and BC architectures, however, evolve differently: In the former, the presence of the injection barrier leads to an overall reduction in the slope of the transfer curves largely independent of  $d_{\text{ins}}$ . This is seen best in the linear regime beyond  $|V_{\text{GS}}| > 20$  V in Fig. 3(a). The BC transfer curves, on the other hand, appear rigidly shifted with respect to each other [Fig. 3(b)] with the magnitude of the shift increasing with the thickness of the dielectric.

To further quantify these observations, we performed a linear fit for each transfer curve in the far linear regime ( $|V_{\text{GS}}| \gg |V_{\text{DS}}|$ ) and used Eq. (1) to extract the apparent threshold voltage  $\bar{V}_{\text{th}}$  and the slope  $\partial I_{\text{DS}}/\partial V_{\text{GS}}$  of the characteristics, which can be recast as an apparent mobility  $\bar{\mu} = L d_{\text{ins}} (V_{\text{DS}} W \epsilon_0 \epsilon_{r,\text{ins}})^{-1} (\partial I_{\text{DS}}/\partial V_{\text{GS}})$ . The resulting apparent threshold voltage  $\bar{V}_{\text{th}}$  and the ratio between the apparent mobilities  $\bar{\mu}$  and  $\mu$  entering the simulation  $\bar{\mu}/\mu$  are given in Figs. 4(a) and 4(b) as a function of the insulator thickness.

The apparent threshold voltage  $\bar{V}_{\text{th}}$  is practically zero without injection barrier [open symbols in Fig. 4(a)] for both devices. In BC devices for  $\Phi = 0.5$  eV one, however, observes an apparent threshold voltage (green hexagons) that significantly shifts to higher voltages with increasing thickness. In strong contrast,  $\bar{V}_{\text{th}}$  in TC devices (squares) remains close to 0 V independently of  $d_{\text{ins}}$ .

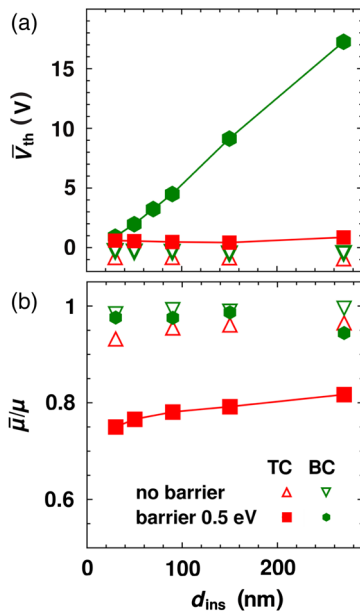


FIG. 4. Apparent threshold voltage  $\bar{V}_{\text{th}}$  (a) and ratio of the apparent mobility to the input mobility (b) for a BC (green down triangles and hexagons) and TC device (red up triangles and squares) as a function of  $d_{\text{ins}}$  for injection barriers of  $\Phi = 0$  (open symbols) and 0.5 eV (filled symbols). The devices have  $L = 5$   $\mu\text{m}$  and  $\mu = 1$   $\text{cm}^2/(\text{V s})$  and are operated at  $V_{\text{DS}} = -20$  V.

As far as the apparent mobility is concerned, the values extracted for a vanishing injection barrier again correspond to the expectation from the GCA [Fig. 4(b), up and down triangles]. Upon increasing the barrier from  $\Phi = 0$  to 0.5 eV (open and filled symbols), the apparent mobility in BC devices remains only marginally smaller than the ideal one; in a TC device, however,  $\bar{\mu}$  is significantly reduced and reaches only 75% of the ideal value at the smallest considered oxide thickness ( $d_{\text{ins}} = 30$  nm).

## V. ORIGIN OF THE ARCHITECTURE-SPECIFIC BEHAVIOR

### A. Threshold voltage

The observed complementary occurrence of either (i) an apparent mobility or (ii) threshold voltage is rooted in the peculiar, architecture-specific potential distribution that is adopted in the vicinity of the injecting source contact [18]. To rationalize first the occurrence of nonzero apparent threshold voltages in BC devices and their nearly zero counterparts in TC OTFTs, it is useful to return to the set of scaled transfer curves shown in Figs. 3(a) and 3(b). For a given gate bias, e.g.,  $V_{\text{GS}} = -10$  V, we can readily see that the BC device with  $d_{\text{ins}} = 30$  nm shown in Fig. 3(b) is clearly in the “on state” [ $\bar{V}_{\text{th}} = 1$  V in Fig. 4(a)]. For  $d_{\text{ins}} = 270$  nm, the device is off [ $\bar{V}_{\text{th}} = 18$  V in Fig. 4(a)]. In that case, essentially the whole potential difference between source and gate drops at the contact and the associated  $V_C$  value approaches the largest possible value, namely  $V_C \sim |V_{\text{GS}}|$  [cf. open circles and dashed line in Fig. 3(d)].

To understand the fundamentally different state the two devices are in, it is useful to consider their initial potential and carrier-density distributions (i.e., the situation right after applying the respective potentials to the electrodes but prior to carrier accumulation in the channel) and to compare them to the distributions assumed in the steady state. The corresponding potentials along the semiconductor-dielectric interface are shown as dashed (initial condition) and solid (steady-state) lines in Fig. 5(a) for the smallest and largest considered thicknesses of the dielectric. Initially (i.e., in the absence of free-charge carriers), the potential in the central region between the contacts must assume the value of the gate potential ( $V_{\text{GS}} = -10$  V) due to the large aspect ratio  $L/d_{\text{ins}}$  of the device [27]. As the potential at the source contact is fixed, there is an inherent potential drop of  $V_{\text{GS}}$  between the contact and the channel [white arrow, Fig. 5(a)]. The smaller  $d_{\text{ins}}$  becomes, the shorter is the distance from the source over which the potential drops from source to gate potential. For  $d_{\text{ins}} = 30$  nm this distance amounts to  $\sim 100$  nm, while it increases by more than an order of magnitude in a device with  $d_{\text{ins}} = 270$  nm (cf. blue and black dashed lines). Associated with the potential drop is an initial gate-induced field. As its strength is proportional to the slope of the potential drop, it is an order of magnitude lower in the 270-nm device than in the

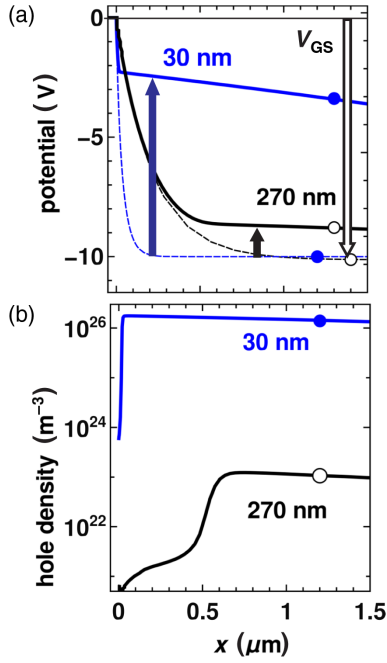


FIG. 5. Evolution of the electrostatic potential (a) in the initial state (dashed lines) and steady state (solid lines) and the steady-state hole density (b) along the organic semiconductor-insulator interface as a function of the distance from the source contact in a BC device at  $V_{GS} = -10$  V,  $V_{DS} = -20$  V, and  $\Phi = 0.5$  eV for different insulator thicknesses  $d_{ins} = 30$  (filled circles) and 270 nm (open circles).

30-nm device. By allowing now an influx of charges, the injected and accumulated charge carriers screen the initial electric field until the steady state is reached. In the 30-nm device, the initial potential drop of  $|V_{GS}| = 10$  V is largely reduced to a remaining voltage of  $V_C = 2$  V in the steady state [cf. blue arrow between dashed and solid lines in Fig. 5(a)]. In this situation, an accumulated carrier density of  $10^{26} \text{ m}^{-3}$  [Fig. 5(b)] gives rise to an appreciable current. In the case of the 270-nm-thick insulator, the field is too weak to sufficiently reshape the barrier and a much smaller number of charges is injected. Because of the weak screening by injected charge carriers, the distance over which the potential in the steady state drops from the source to the gate potential is only weakly reduced. Hence, with ca. 9 V the steady state  $V_C$  remains close to the initial  $|V_{GS}|$  value of 10 V. Concomitantly, the charge density in the region between the contact and the conductive channel is particularly strongly depleted. In addition, the charge density in the channel region is reduced; it is more than 3 orders of magnitude smaller than for the 30-nm device [Fig. 5(b)]. This is significantly less than expected from the GCA expression (2), which—disregarding the contact resistance—would have only implied a decrease by a factor of 9 as a consequence of the reduced capacitance of the insulator.

The behavior that  $V_C$  closely follows  $V_{GS}$  at small gate biases due to a strongly reduced carrier injection is observed for all BC devices [cf. Fig. 3(d)] at small gate biases. Upon increasing  $|V_{GS}|$  the rise of  $V_C$ , however, slows down. The voltage at which this becomes relevant depends strongly on the thickness of the gate insulator. The point at which  $V_{GS}$  reaches the value of the apparent threshold voltage is denoted by large crosses in the curves in Fig. 3(d), where it should be kept in mind that  $\bar{V}_{th}$  is merely a fitting parameter in the linear regime of the transfer characteristics. At this point, the difference between  $V_C \cong |V_{GS}|$  and the actual evolution of  $V_C(V_G)$  has become appreciable. Thicker insulator layers require larger  $V_C$  values to provide a large-enough barrier-shaping field to inject a sufficient number of carriers for reaching that situation. Thus, the gate-voltage range over which  $V_C \cong |V_{GS}|$  applies increases with the thickness of the dielectric. In that sense, the apparent threshold voltage [indicated by large crosses in Fig. 3(d)] can be associated with the minimal gate bias necessary to overcome the injection barrier, as suggested in Ref. [19].

In TC architectures, the threshold voltage does not visibly shift when modifying the insulator thickness. This roots in the fact that the above-described dependence of the gate field on  $d_{ins}$  (and on the present aspect ratio) is, for the given device dimensions, i.e., semiconductor thickness  $d_{OSC} = 30$  nm and channel length  $L = 5 \mu\text{m}$ , and a mobility of  $1 \text{ cm}^2/(\text{Vs})$  much less pronounced. Consequently, the field is sufficiently large to permit injection across a barrier of 0.5 eV for all  $d_{ins}$ .

## B. Apparent mobility

To understand why there is a reduction in the apparent mobility in the linear regime in TC devices that does not occur for the BC architecture, it is useful to track the impact of the  $V_{GS}$ -dependent  $V_C$  in the GCA expression [cf. Eq. (1)]. Accounting for the fact that the potential at the channel entrance is not given by the source potential but rather by the source potential reduced by  $V_C$ , the external biases in Eq. (1) are replaced by  $V_{DS} - V_C$  and  $V_{GS} - V_C$ , respectively. Considering that the threshold voltage  $V_{th}^0$  is set to zero (see Sec. II), the current reads in the linear regime

$$I_{DS} = \frac{W \epsilon_0 \epsilon_{r,ins}}{L d_{ins}} \mu \left( V_{GS} - V_C - \frac{(V_{DS} - V_C)}{2} \right) (V_{DS} - V_C). \quad (4)$$

This implies for the slope of the transfer characteristic, and, thus, for the apparent mobility

$$\frac{\partial I_{DS}}{\partial V_{GS}} = \frac{W \epsilon_0 \epsilon_{r,ins}}{L d_{ins}} \mu \left[ V_{DS} - V_C - (V_{GS} - V_C) \frac{\partial V_C}{\partial V_{GS}} \right]. \quad (5)$$

The first summation term in Eq. (5) is inherited from the ideal GCA and relates to the actual mobility of the used material. The second term simply corrects  $V_{DS}$  for the presence of  $V_C$ , while the third summation term accounts for the change of  $V_C$  with  $V_{GS}$ . It is important to stress that  $\partial V_C/\partial V_{GS}$  cannot be neglected *a priori*; in fact, it is this latter term that explains the difference between the slopes of the TC and BC transfer curves [Figs. 3(a) and 3(b)]: When operating TC devices in the linear regime, i.e., at  $|V_{GS}|$  exceeding  $|V_{DS}| = 20$  V, the contact potential  $V_C$  depends weakly on  $d_{ins}$  [Fig. 3(c)] and increases only slightly with  $V_{GS}$  [seen best for the magnified curves in Fig. 3(c)]. As  $V_C$  is approximately constant, the third term containing the derivative of  $V_C$  with respect to  $V_{GS}$  can, indeed, be neglected. Then, the overall slope of the transfer curve is reduced due to the second term in Eq. (5) being proportional to  $V_C$ . Because of the  $V_{GS}$ - and largely  $d_{ins}$ -independent  $V_C$ , this reduced slope can be simply interpreted in terms of an apparent, constant mobility.

Conversely, for BC we find a  $V_C$  that profoundly varies with  $V_{GS}$  [Fig. 3(d)]. Thus, the contribution  $(V_{GS} - V_C)(\partial V_C/\partial V_{GS})$ , extracted from the  $V_C(V_{GS})$  curves in Fig. 3(d) is nonnegligible. Given this strong dependence of  $V_C$  on both  $d_{ins}$  and on  $V_{GS}$ , it appears counterintuitive that the BC device recovers not only a linear transfer curve, but also the ideal GCA-predicted slope. Remarkably, though, in the linear regime, i.e., where  $|V_{GS}|$  exceeds  $|V_{DS}| + \bar{V}_{th}$  [the corresponding values are indicated by vertical bars in Fig. 3(d)],  $V_{GS}(\partial V_C/\partial V_{GS})$  is negative and almost completely compensates for  $V_C$  in Eq. (5) so that the “ideal” GCA slope is recovered despite the enormous,  $V_{GS}$ -dependent values of  $V_C$ .

This implies for the analysis of experimentally obtained transfer curves that the apparent dependence of the effective mobilities on the gate bias [3,16,35] arises not only due to a field- and concentration-dependent intrinsic mobility, but also due to the  $V_{GS}$  dependence of the contact voltage. The latter fact poses the complication that any correction for  $V_C$  could be, at least in part, counteracted due to the contribution from  $(V_{GS} - V_C)(\partial V_C/\partial V_{GS})$ . For the TC devices, the contact voltage extracted in the linear regime is nearly independent of  $V_{GS}$ . The effect of practically constant-contact voltages on the  $I$ - $V$  characteristic can be straightforwardly accounted for by following, e.g., the procedure outlined in Ref. [36]. However, a method accounting for a possible compensation due to  $(V_{GS} - V_C)(\partial V_C/\partial V_{GS})$  is, to the best of our knowledge, not yet available.

## VI. DEPENDENCE ON MATERIAL PARAMETERS

### A. Dielectric constant

So far, the insulator capacitance has been exclusively varied by means of the film thickness. Now we turn to the equivalent route of varying instead the dielectric constant

$\epsilon_{r,ins}$ . We start out from  $\epsilon_{r,ins} = 3.9$  for  $\text{SiO}_2$  as the commonly applied “reference dielectric.” To be able to directly compare to the results obtained from the thickness variation, we further employ values obtained by consecutively multiplying the reference value by a factor of 3, i.e.,  $3\epsilon_{r,\text{SiO}_2} = 11.7$  and  $9\epsilon_{r,\text{SiO}_2} = 35.1$ . Together with film thicknesses of  $d_{ins} = 30, 90,$  and  $270$  nm, the same capacitance value can be realized. Such  $\epsilon_{r,ins}$  values closely correspond to dielectric constants of insulating layers employed in OTFTs: Aluminum oxide  $\epsilon_r = 8$  [15] and, e.g., cyanoethylated poly(vinyl alcohol) with  $\epsilon_r = 12.6$  [37] are close to 11.7, while 35.1 is close to  $\text{TaO}_2$  and  $\text{HfO}_2$  ( $\sim 25$ ) [15,38]. We also incorporate  $\epsilon_r = 2.7$  in our study to account for polymer dielectrics, pursued to realize flexible devices, whose dielectric constants are as low as  $\epsilon_r = 2$  [15]. However, in the present context the chosen values only serve the purpose of illustrating the fundamental aspects related to the interplay of the gate capacitance and injection. In passing, we also note that systematic experimental investigations revealed that upon increasing  $\epsilon_{r,ins}$  the interaction between an increasingly polar dielectric surface and the OSC profoundly decreases the mobility at the OSC-insulator interface [39,40]—an effect that can, at least in part, be counteracted by modifying insulator surfaces, e.g., by self-assembled monolayers [12,15].

In a first step, we simultaneously vary both  $\epsilon_{r,ins}$  and  $d_{ins}$  by a factor of 3 and 9, so that the capacitance per unit area is kept at the value of  $C' = 115$  nFcm<sup>-2</sup> as in the above-discussed devices with  $d_{ins} = 30$  nm and  $\epsilon_{r,ins} = \epsilon_{r,\text{SiO}_2}$  (*vide supra*). As expected, the characteristics of the transistors coincide when the injection barrier is absent (not shown). To explore whether this is also true for a substantial injection barrier, we collected the scaled output curves of TC and BC devices for an injection barrier of 0.5 eV in Fig. 6. In the case of a TC OTFT, again all output curves coincide [Fig. 6(a)], albeit at currents that are significantly decreased compared to the GCA case. This means that for TC devices, reducing the thickness of the gate dielectric or increasing its dielectric constants by an equivalent degree has exactly the same impact and all that counts in TC devices is the gate capacitance. In sharp contrast, for BC devices, curves with the same ratio  $\epsilon_{r,ins}/d_{ins}$  are distinctly different. As in the systematic thickness variation at a constant  $\epsilon_{r,ins}$  performed above, we get lesser current when going to larger insulator thicknesses [Fig. 6(b)]. The accordingly scaled  $\epsilon_{r,ins}$  is partially counteracting this effect, as can be seen from the comparison of the 270-nm devices with  $\epsilon_{r,ins} = 3.9$  (circles) and 35.1 (red, right triangles), but cannot fully compensate this loss in current.

The larger-than-expected dependence of the current on  $\epsilon_{r,ins}$  in BC devices is a consequence of the orientation of the injecting facet of the electrode with respect to the semiconductor interface in the BC OTFTs. There, injection is enabled by field components *parallel* to the

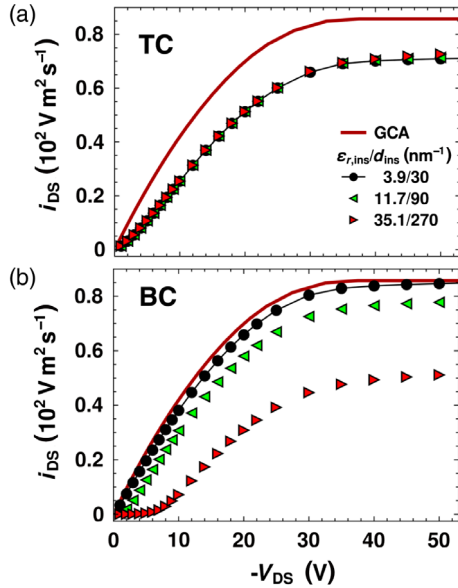


FIG. 6. (a),(b) Scaled output curves  $i_{DS}(V_{DS})$  for an injection barrier  $\Phi = 0.5$  eV for TC (a) and BC (b) OTFTs sharing the same capacitance per unit area,  $C' = 115$  nF cm $^{-2}$  realized with different insulator thicknesses and  $\epsilon_{r,ins}$ . In all cases, the result of the gradual channel approximation (red, solid line) is shown for comparison; the devices are operated at  $V_{GS} = -35$  V.

OSC-insulator interface. Importantly, since the field near the source electrode of a BC device is inhomogeneous, the relative orientation of the field and, thus, the strength of the lateral and vertical field components is not straightforwardly determined by the gate capacitance alone. A

rationale for this based on a simplified model system is provided in the Appendix. To comprehend the additional influence of the dielectric constant on injection, we proceed with a systematic variation of  $\epsilon_{r,ins}$  at a given insulator thickness. We show in Figs. 7(a) and 7(b) the output and transfer characteristics of BC devices for different values of  $\epsilon_{r,ins}$  at a fixed insulator thickness of  $d_{ins} = 270$  nm.

All output curves show a similarly pronounced S shape in the linear regime [Fig. 7(a)]. The scaled current rises in the saturation regime ( $|V_{DS}| > 20$  V) with increasing  $\epsilon_{r,ins}$ , except for the smallest value of 2.7. Note that the device with  $\epsilon_{r,ins} = 2.7$  is the only one in which the dielectric constant of the insulating layer is smaller than that of the organic semiconductor  $\epsilon_{r,OSC} = 3.4$ . In the case of the transfer characteristics, all curves show a similar turn-on behavior [Fig. 7(b)]. The small increase in the apparent threshold due an enlarged  $\epsilon_{r,ins}$  is far less pronounced compared to the variation of the thickness of the dielectric layer [cf. Fig 3(b)]. To explain this, we turn to the local field and charge distribution near the source contact in the steady state for  $V_{GS} = -35$  V, i.e., for a point of operation in which all considered devices are in an on state. In Fig. 7(c), this field distribution is represented by the lateral evolution of the potential (i) from the source into the channel and (ii) perpendicular to the channel from the injecting source facet 10 nm towards the gate [inset in Fig. 7(c)]. The corresponding charge density along the channel is given in Fig. 7(d). Interestingly, when going from  $\epsilon_{r,ins} = 3.9$  (open circles) to 35.1 (green triangles) for the  $d_{ins} = 270$  nm, the potential drop at the contact is only slightly reduced and profoundly different from the  $d_{ins} = 30$  nm,  $\epsilon_{r,ins} = 3.9$

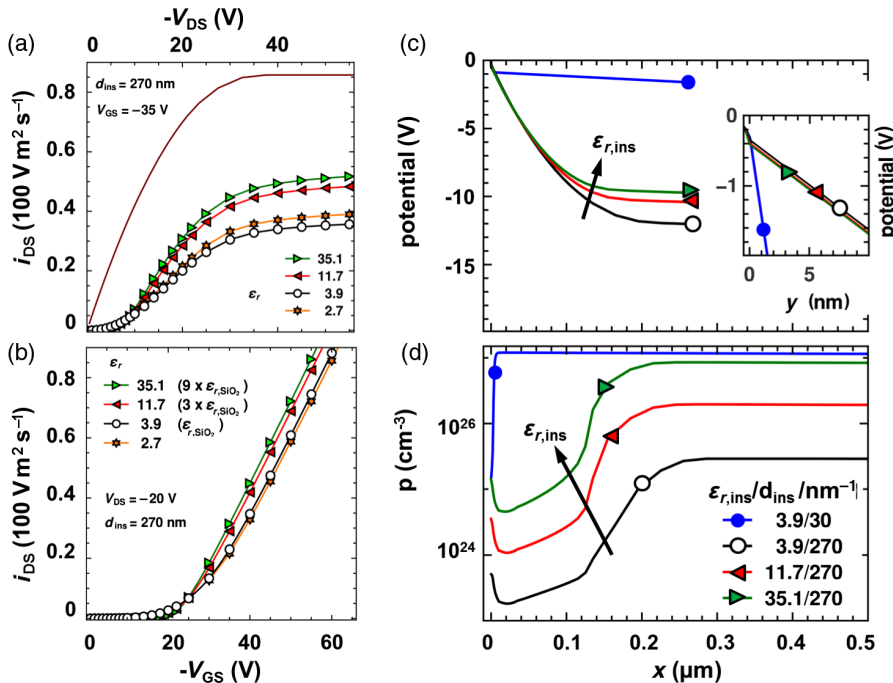


FIG. 7 (a),(b) Scaled output  $i_{DS}(V_{DS})$  (a) and transfer curves  $i_{DS}(V_{GS})$  (b) of BC devices for varying dielectric constants  $\epsilon_{r,ins}$  at the insulator thickness  $d_{ins} = 270$  nm and an injection barrier of 0.5 eV. In (b), the value in brackets indicates the multiplication factor of  $\epsilon_{r,ins}$  with respect to the reference value of 3.9 corresponding to SiO $_2$ . (c) Lateral potential distribution at the OSC-insulator interface from the position of the source contact ( $x = 0$ ) for a BC device at  $V_{GS} = -35$  V. Shown are curves for varying  $\epsilon_{r,ins}$  at  $d_{ins} = 270$  nm (open circles, left and right triangles) in comparison to  $\epsilon_{r,ins} = 3.9$  and  $d_{ins} = 30$  nm (filled circles). Analogously, the inset shows the vertical potential distribution at the position of the source contact starting at the OSC-insulator interface ( $y = 0$ ). (d) Charge-carrier density along the OSC-insulator interface from the position of the source contact ( $x = 0$ ) for the same devices shown in panel (c).

device [filled circles in Fig. 7(c) and in the inset]. Similarly, the low-density region next to the source contact reduces that somewhat in size, but is essentially preserved [cf. Figs. 7(c) and 7(d)]. Nevertheless, the charge density increases by almost 2 orders of magnitude when enhancing  $\epsilon_{r,\text{ins}}$  by a factor of 9 [cf. open circles and green triangles in Fig. 7(d)]. An important consequence of that is that the charge density for  $\epsilon_{r,\text{ins}} = 35.1$  (open circles) in the channel region, i.e., beyond the low-density region, approaches the density associated with the thin device ( $d_{\text{ins}} = 30$  nm,  $\epsilon_{r,\text{ins}} = 3.9$ ; filled circles). This illustrates that the orientation of the electric field near the source contact is strongly dependent on the insulator thickness; the larger  $d_{\text{ins}}$ , the smaller the contribution of the vertical field component becomes. The resulting change in field orientation cannot be simply reversed by increasing  $\epsilon_{r,\text{ins}}$ . Rather, an increase in  $\epsilon_{r,\text{ins}}$  slightly enlarges the lateral field component and, thus, the injected current. The evaluation of the curves in Fig. 7(c) shows an increase in field strength of 35% when going from  $\epsilon_{r,\text{ins}} = 3.9$  to 35.1.

From Fig. 7(b), we find that the apparent mobility slightly increases with  $\epsilon_{r,\text{ins}}$ . In experiments, the latter effects will, however, be most likely obscured by the above-mentioned interaction between the increasingly polar surface and the semiconductor [39,40].

### B. Mobility and injection barrier

The impact of injection on the transistor characteristics is crucially determined by the actual current demand of the channel (cf. Sec. II). We, thus, briefly explore how (i) the mobility (determining the current demand) and (ii) the injection barrier (reflecting the ability of the contact to supply this demand) affect the general picture described above.

In Fig. 8(a), we show the scaled transfer curves for  $d_{\text{ins}} = 270$  nm, i.e., for the film thickness with the largest and most distinguished injection-induced effect in a BC architecture, as a function of the injection barrier. Interestingly, the situation for an injection barrier of 0.3 eV (red hexagons) largely resembles the ideal case associated with a vanishing barrier (blue diamonds). Only when increasing the injection barrier to 0.5 eV, the above-mentioned mobility reduction in TC devices [circles versus blue diamonds, left panel in Fig. 8(a)] and threshold voltage shifts in BC devices [circles versus blue diamonds, right panel in Fig. 8(a)] become significant. In Fig. 8(b), the scaled transfer curves are shown for different mobilities. Note that, even in the ideal case, we need to divide the current not only by the capacitance per unit area, but also by the ratio of the mobilities  $\mu/\mu_{\text{ref}}$  with  $\mu_{\text{ref}} = 1$  cm<sup>2</sup>/(V s) to obtain equivalent curves and to determine whether the expectation from the GCA [Eq. (1)] is altered due to injection. With increasing nominal mobility, the slope in the linear regime ( $|V_{\text{GS}}| > 20$  V) of the TC device is reduced [left panel in Fig. 8(b)]. I.e., the relative decrease

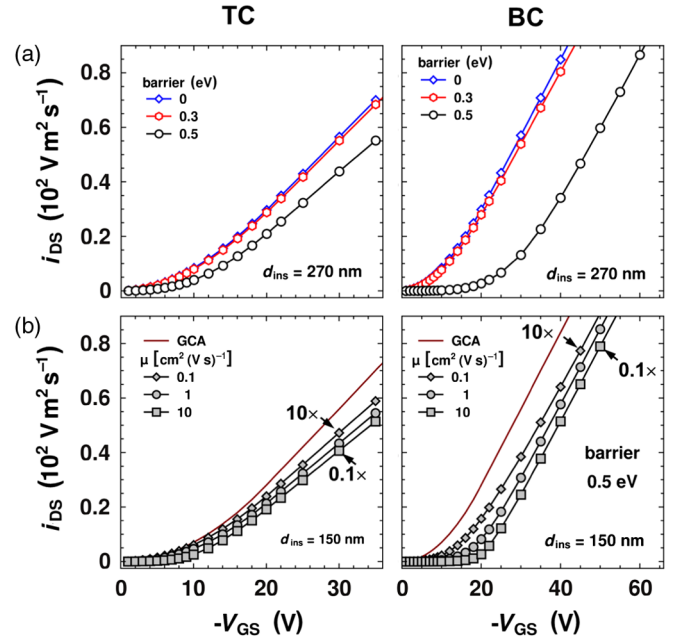


FIG. 8. Comparison of scaled transfer curves of a TC and a BC device with  $\epsilon_{r,\text{ins}} = 3.9$  at  $V_{\text{DS}} = -20$  V with different injection barriers and charge mobilities. (a)  $i_{\text{DS}}$  ( $V_{\text{GS}}$ ) for  $\mu = 1$  cm<sup>2</sup>/V s and  $d_{\text{ins}} = 270$  nm for injection barrier heights of 0, 0.3, and 0.5 eV. (b)  $i_{\text{DS}}\mu_{\text{ref}}/\mu(V_{\text{GS}})$  for an injection barrier of 0.5 eV and  $d_{\text{ins}}$  for the mobility values  $\mu = 0.1, 1$  ( $\mu_{\text{ref}}$ ), and 10 cm<sup>2</sup>/V s. To be able to compare the mobility-dependent transfer curves, all curves are scaled with an additional factor containing the ratio  $\mu/\mu_{\text{ref}}$ . This factor is indicated at the corresponding curve.

of the apparent mobility compared to the actual one is more pronounced for higher mobilities. This is not surprising, as a higher mobility means a larger current in the channel and, consequently, requires an increased potential drop at the contact to ensure the injection of a sufficient number of carriers. In addition, for the largest considered mobility  $\mu = 10$  cm<sup>2</sup>/(V s) one observes a small threshold voltage shift of  $\bar{V}_{\text{th}} \approx 1$  V (at  $d_{\text{ins}} = 150$  nm) and  $\approx 2$  V (at  $d_{\text{ins}} = 270$  nm). Thus, the device dimensions in combination with the large mobility require a current that, at least for small biases, cannot be provided by the contact in a TC OTFT.

In case of a BC device, the threshold-voltage shift steadily increases with the mobility [right panel in Fig. 8(b)]. A closer inspection reveals further that also in a BC device the apparent mobility is slightly mobility dependent: For the smallest mobility of  $\mu = 0.1$  cm<sup>2</sup>/(V s) considered, the apparent mobility is  $0.95 \mu$ , while for the higher values the apparent mobility is as high as  $0.99 \mu$ .

## VII. CONCLUSIONS

In conclusion, we have shown that a limited ability of the contact to inject charges contributes to an apparently lowered mobility and an apparent threshold voltage. In

TC architectures, a lowering of the apparent mobility is the dominant contribution. In contrast, in BC devices no such injection-induced mobility lowering in the linear regime is observed, despite the fact that the contact voltage, i.e., the potential drop at the injecting contact, is strongly dependent on the gate bias. This is the consequence of the fact that the actual value of the apparent mobility results from a correction due to the contact voltage and a second correction caused by the gate-bias dependence of the contact voltage. The latter correction can, at least partially, compensate the impact of the contact voltage. Additionally, we show that injection-related shifts in the apparent threshold voltage appear in BC devices with increased insulator thickness; for mobilities as high as  $1 \text{ cm}^2/(\text{Vs})$  values exceeding 10 V can be reached. As a consequence, when trying to interpret experimentally obtained transfer characteristics, observed shifts in the threshold voltage, especially in BC transistors, can arise, at least in part, due to the presence of an injection barrier.

In the case of a substantial injection barrier, here 0.5 eV, the current in a BC transistor is much stronger controlled by the insulator thickness than by its dielectric constant. In contrast, TC devices show—as one would intuitively expect—the same current for a given insulator capacitance per unit area, independent of the actual values for the dielectric constant or the thickness. This is the manifestation of the fact that injection into a BC device relies on the field component oriented along the channel rather than the one perpendicular to the OSC-insulator interface. Because of the marked inhomogeneity of the electric field near the source, the strengths of the lateral field (enabling injection) and of the vertical field perpendicular to the channel (allowing charge accumulation) strongly change with increasing film thickness. An enlargement of the dielectric constant, however, slightly enhances the lateral, injection-aiding field without being able to change the strength of the vertical field component near the contact.

The above-mentioned effects intensify with increasing mobility and injection barrier. Vice versa, a reduction of the injection barrier, e.g., to 0.3 eV, increasingly suppresses threshold voltage shifts and mobility lowering.

## ACKNOWLEDGMENTS

Financial support has been provided from the Austrian Science Fund through the FWF Elise Richter Fellowship (V317-N20). A. F. F. has received funding from the European Union Seventh Framework Programme under Grant Agreement No. 607232 (THINFACE).

## APPENDIX: INEQUIVALENCE OF DIELECTRIC CONSTANT AND INSULATOR THICKNESS VARIATION FOR INHOMOGENEOUS FIELDS

Here, we aim at developing a rationale for the *a priori* unexpected observation that either reducing  $d_{\text{ins}}$  by a

certain factor or increasing  $\epsilon_{r,\text{ins}}$  by the same factor does not yield the same current in BC transistors. Rather, BC devices with a given insulator capacitance per unit area possess a potential distribution that depends on the value of  $\epsilon_{r,\text{ins}}$ . Already in the initial state, potential distributions in devices with the same capacitance per unit area are not necessarily independent of the choice of  $\epsilon_{r,\text{ins}}$ . This is a straightforward consequence of the marked inhomogeneity of the electric field in the BC geometry.

To rationalize this from a purely electrostatic point of view, we turn to the textbook example of a plate capacitor sandwiching a dielectric, insulating material. Between infinitely extended planar electrodes, an externally applied bias causes a homogeneous electric field in the insulator. This homogeneity is, of course, preserved upon changing either  $\epsilon_{r,\text{ins}}$  or the electrode separation. If the ratio between the latter quantities is fixed, also the capacitance stays constant.

If, instead, the top electrode possesses a hole [shown in Fig. 9], the electric field becomes inhomogeneous in the

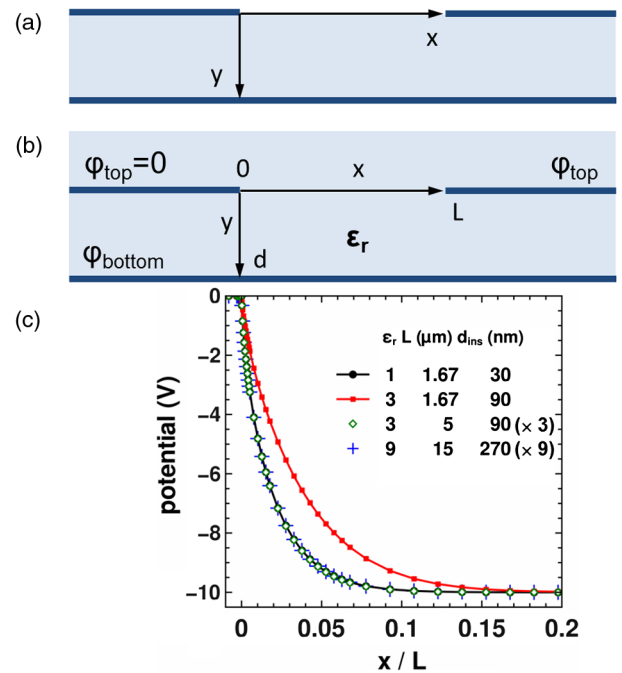


FIG. 9. (a) Two-dimensional cross section of a plate capacitor with a hole in the top electrode, filled with a dielectric medium with a dielectric constant of  $\epsilon_r$ . (b) As in (a), with vacuum replaced by the dielectric medium to omit an interface between two dielectric media. The hole has a radius  $L$  and the separation of the electrodes is  $d$ . The resulting two-dimensional cross section is reminiscent of the BC geometry with the top electrodes put at the same potential. (c) Potential in the plane of the top electrode for four cases sharing the same capacitance per unit area. Starting out from a reference case (circles), either are all dimensions scaled as the dielectric constant (factor 3, diamonds; factor 9, crosses) or only the separation of the electrodes (factor 3, rectangles) by keeping the hole radius constant. The calculations are carried out for the cross section shown in (b) with an applied bias of 10 V.

vicinity of the hole. For an in-depth discussion of the field distribution, the reader may refer to Ref. [41]. Note that the corresponding cross section shown in Fig. 9 is reminiscent of that belonging to the transistor architecture: In the case of a BC device, the capacitor contains one, in the TC case a sequence of two dielectric layers (the gate dielectric and the organic semiconductor). When going from the remote area towards the center of such a capacitor, the local orientation of the electric field changes. This orientation is further affected by the value of  $\epsilon_{r,\text{ins}}$ . Inspired by the discussion of the transistor, the question arises of how the extensions of this plate capacitor ought to be rescaled to preserve (i) the capacitance and (ii) the orientation of the local electric field. We will answer this question in turning to a related system, shown in Fig. 9(b), in which the top electrode is immersed in a dielectric medium. This obliterates the need to consider an interface between vacuum and the dielectric and, thus, simplifies the following considerations. In the model system, the radius of the hole is denoted as  $L$ , the vertical separation between the electrodes as  $d$ , and a bias of  $V = \psi_{\text{top}} - \psi_{\text{bottom}}$  is applied, i.e., the potentials  $\psi$  at the electrodes are fixed to  $\psi_{\text{top}}$  and  $\psi_{\text{bottom}}$ . Starting out from a given  $L$  and  $d$ , the field orientation is reflected by the ratio  $(\partial\psi/\partial y)/(\partial\psi/\partial x)$ . To explore the impact of changing the extensions of the capacitor, it is convenient to introduce dimensionless coordinates  $x'' = x/L$  and  $y'' = y/d$ . The preservation of field orientation corresponds to the condition

$$\frac{\partial\psi}{\partial y} = \frac{\partial\psi}{\partial y''} \frac{d}{L}.$$

That means that the field orientation is kept only if the separation  $d$  and the hole radius  $L$  are stretched simultaneously by the same factor. To illustrate this conceptual aspect, we numerically calculated the potential distribution for a cross section shown in Fig. 9(b) with a starting geometry of  $d = 30$  nm,  $L = 1.67$   $\mu\text{m}$ ,  $\epsilon_{r,\text{ins}} = 1$ , and a bias of  $V = 10$  V. All further cases kept the ratio  $\epsilon_{r,\text{ins}}/d$  constant. Figure 9(c) compares the resulting potentials in the plane of the top electrode by plotting  $\psi$  as a function of the dimensionless  $x$  coordinate  $x/L$ . Enlarging  $\epsilon_{r,\text{ins}}$  by a factor of  $n$  and, at the same time, enlarging all device dimensions (including  $d$ ,  $L$ , and the electrode extension) by the same factor keeps the potential distribution unchanged, i.e., for  $n = 1, 3, 9$  (filled circles, open diamonds, crosses). When, however, restricting the stretch to the separation of the electrode  $d$  (for  $n = 3$ , rectangles), the  $x$  component of the field is differently altered than the  $y$  component. This results in a shallower slope of the potential in the plain of the top electrode (cf. filled circles and rectangles).

This implies for an OTFT that any variation of the ratio  $\epsilon_{r,\text{ins}}/d_{\text{ins}}$  without a corresponding change in  $L$  causes a

nonequivalent change in the field components. As, due to a constant channel length, the starting conditions inherently depend on  $\epsilon_{r,\text{ins}}/d$ , also the steady-state potential distributions for a given capacitance  $C'$  cannot be expected to coincide.

- 
- [1] D. Braga and G. Horowitz, High-performance organic field-effect transistors, *Adv. Mater.* **21**, 1473 (2009).
  - [2] H. Klauk, Organic thin-film transistors, *Chem. Soc. Rev.* **39**, 2643 (2010).
  - [3] F. Ante, D. Kälblein, U. Zschieschang, T. Canzler, A. Werner, K. Takimiya, M. Ikeda, T. Sekitani, T. Someya, and H. Klauk, Contact doping and ultrathin gate dielectrics for nanoscale organic thin-film transistors, *Small* **7**, 1186 (2011).
  - [4] B. Stadlober, U. Haas, H. Gold, A. Haase, G. Jakopic, G. Leising, N. Koch, S. Rentenberger, and E. Zojer, Orders-of-magnitude reduction of the contact resistance in short-channel hot embossed organic thin film transistors by oxidative treatment of Au-electrodes, *Adv. Funct. Mater.* **17**, 2687 (2007).
  - [5] M. Leufgen, A. Lebib, T. Muck, U. Bass, V. Wagner, T. Borzenko, G. Schmidt, J. Geurts, and L. W. Molenkamp, Organic thin-film transistors fabricated by microcontact printing, *Appl. Phys. Lett.* **84**, 1582 (2004).
  - [6] M. Halik, H. Klauk, U. Zschieschang, G. Schmid, C. Dehm, M. Schütz, S. Maisch, F. Effenberger, M. Brunnbauer, and F. Stellacci, Low-voltage organic transistors with an amorphous molecular gate dielectric, *Nature (London)* **431**, 963 (2004).
  - [7] T. Sekitani, U. Zschieschang, H. Klauk, and T. Someya, Flexible organic transistors and circuits with extreme bending stability, *Nat. Mater.* **9**, 1015 (2010).
  - [8] U. Zschieschang, M. J. Kang, K. Takimiya, T. Sekitani, T. Someya, T. W. Canzler, A. Werner, J. Blochwitz-Nimoth, and H. Klauk, Flexible low-voltage organic thin-film transistors and circuits based on C10-DNTT, *J. Mater. Chem.* **22**, 4273 (2012).
  - [9] N. A. Minder, S. Ono, Z. Chen, A. Facchetti, and A. F. Morpurgo, Band-like electron transport in organic transistors and implication of the molecular structure for performance optimization, *Adv. Mater.* **24**, 503 (2012).
  - [10] Y. Yuan, G. Giri, A. L. Ayzner, A. P. Zoombelt, S. C. B. Mannsfeld, J. Chen, D. Nordlund, M. F. Toney, J. Huang, and Z. Bao, Ultra-high mobility transparent organic thin film transistors grown by an off-centre spin-coating method, *Nat. Commun.* **5**, 3005 (2013).
  - [11] C. Reese and Z. Bao, Organic single-crystal field-effect transistors, *Mater. Today* **10**, 20 (2007).
  - [12] O. Acton, G. Ting, H. Ma, J. W. Ka, H.-L. Yip, N. M. Tucker, and A. K. -Y. Jen,  $\pi$ - $\sigma$ -phosphonic acid organic monolayer/sol-gel hafnium oxide hybrid dielectrics for low-voltage organic transistors, *Adv. Mater.* **20**, 3697 (2008).
  - [13] J. H. Cho, J. Lee, Y. Xia, B. Kim, Y. He, M. J. Renn, T. P. Lodge, and C. D. Frisbie, Printable ion-gel gate dielectrics for low-voltage polymer thin-film transistors on plastic, *Nat. Mater.* **7**, 900 (2008).

- [14] M. Zirkl, A. Haase, A. Fian, H. Schön, C. Sommer, G. Jakopic, G. Leising, B. Stadlober, I. Graz, N. Gaar, R. Schwödianer, S. Bauer-Gogonea, and S. Bauer, Low-voltage organic thin-film transistors with high- $k$  nanocomposite gate dielectrics for flexible electronics and optothermal sensors, *Adv. Mater.* **19**, 2241 (2007).
- [15] R. Ponce Ortiz, A. Facchetti, and T. J. Marks, High- $k$  organic, inorganic, and hybrid dielectrics for low-voltage organic field-effect transistors, *Chem. Rev.* **110**, 205 (2010).
- [16] F. Ante, D. Kälblein, T. Zaki, U. Zschieschang, K. Takimiya, M. Ikeda, T. Sekitani, T. Someya, J. N. Burghartz, K. Kern, and H. Klauk, Contact resistance and megahertz operation of aggressively scaled organic transistors, *Small* **8**, 73 (2012).
- [17] A. Hoppe, D. Knipp, B. Gburek, A. Benor, M. Marinkovic, and V. Wagner, Scaling limits of organic thin film transistors, *Org. Electron.* **11**, 626 (2010).
- [18] M. Gruber, E. Zojer, F. Schürer, and K. Zojer, Impact of materials versus geometric parameters on the contact resistance in organic thin-film transistors, *Adv. Funct. Mater.* **23**, 2941 (2013).
- [19] J. J. Brondijk, F. Torricelli, E. C. P. Smits, P. W. M. Blom, and D. M. de Leeuw, Gate-bias assisted charge injection in organic field-effect transistors, *Org. Electron.* **13**, 1526 (2012).
- [20] C. H. Kim, Y. Bonnassieux, and G. Horowitz, Fundamental benefits of the staggered geometry for organic field-effect transistors, *IEEE Electron Device Lett.* **32**, 1302 (2011).
- [21] B. Lüssem, M. L. Tietze, H. Kleemann, C. Hoßbach, J. W. Bartha, A. Zakhidov, and K. Leo, Doped organic transistors operating in the inversion, and depletion regime, *Nat. Commun.* **4**, 2775 (2013).
- [22] M. Gruber, F. Schürer, and K. Zojer, Relation between injection barrier and contact resistance in top-contact organic thin-film transistors, *Org. Electron.* **13**, 1887 (2012).
- [23] C. H. Kim, O. Yaghmazadeh, D. Tondelier, Y. B. Jeong, Y. Bonnassieux, and G. Horowitz, Capacitive behavior of pentacene-based diodes: Quasistatic dielectric constant and dielectric strength, *J. Appl. Phys.* **109**, 083710 (2011).
- [24] P. S. Davids, I. H. Campbell, and D. L. Smith, Device model for single carrier organic diodes, *J. Appl. Phys.* **82**, 6319 (1997).
- [25] E. J. Meijer, C. Tanase, P. Blom, E. van Veenendaal, B.-H. Huisman, D. M. de Leeuw, and T. M. Klapwijk, Switch-on voltage in disordered organic field-effect transistors, *Appl. Phys. Lett.* **80**, 3838 (2002).
- [26] The range has been chosen to cover injection barriers prominently encountered in literature, for the fruit-fly combination pentacene-Au values of ca. 0.5 eV have been frequently reported: (a) F. Amy, C. Chan, and A. Kahn, Polarization at the gold/pentacene interface, *Org. Electron.* **6**, 85 (2005); (b) N. J. Watkins, L. Yan, and Y. Gao, Electronic structure symmetry of interfaces between pentacene and metals, *Appl. Phys. Lett.* **80**, 4384 (2002); (c) L. Diao, C. D. Frisbie, D. D. Schroepfer, and P. P. Ruden, Electrical characterization of metal/pentacene contacts, *J. Appl. Phys.* **101**, 014510 (2007).
- [27] S. K. Possanner, K. Zojer, P. Pacher, E. Zojer, and F. Schürer, Threshold voltage shifts in organic thin-film transistors due to self-assembled monolayers at the dielectric surface, *Adv. Funct. Mater.* **19**, 958 (2009).
- [28] T. Minari, T. Miyadera, K. Tsukagoshi, Y. Aoyagi, and H. Ito, Charge injection process in organic field-effect transistors, *Appl. Phys. Lett.* **91**, 053508 (2007).
- [29] R. A. Street and A. Salleo, Contact effects in polymer transistors, *Appl. Phys. Lett.* **81**, 2887 (2002).
- [30] N. Tessler and Y. Roichman, Two-dimensional simulation of polymer field-effect transistor, *Appl. Phys. Lett.* **79**, 2987 (2001).
- [31] G. Horowitz, *Charge Transport in Oligomers*, in *Organic Field-Effect Transistors*, edited by Z. Bao and J. Locklin (Taylor & Francis, New York, 2007), Chap. 2.2.
- [32] P. V. Necliudov, M. S. Shur, D. J. Gundlach, and T. N. Jackson, Contact resistance extraction in pentacene thin film transistors, *Solid State Electron.* **47**, 259 (2003).
- [33] S. Scheinert and G. Paasch, Interdependence of contact properties and field-and density-dependent mobility in organic field-effect transistors, *J. Appl. Phys.* **105**, 014509 (2009).
- [34] Y. Roichman and N. Tessler, Structures of polymer field-effect transistor: Experimental and numerical analyses, *Appl. Phys. Lett.* **80**, 151 (2002).
- [35] A. Benor and D. Knipp, Contact effects in organic thin film transistors with printed electrodes, *Org. Electron.* **9**, 209 (2008).
- [36] R. Di Pietro, D. Venkateshvaran, A. Klug, E. J. W. List-Kratochvil, A. Facchetti, H. Sirringhaus, and D. Neher, Simultaneous extraction of charge density dependent mobility and variable contact resistance from thin film transistors, *Appl. Phys. Lett.* **104**, 193501 (2014).
- [37] S. H. Kim, S. Y. Yang, K. Shin, H. Jeon, J. W. Lee, K. P. Hong, and C. E. Park, Low-operating-voltage pentacene field-effect transistor with a high-dielectric-constant polymeric gate dielectric, *Appl. Phys. Lett.* **89**, 183516 (2006).
- [38] A. F. Stassen, R. W. I. de Boer, N. N. Iosad, and A. F. Morpurgo, Influence of the gate dielectric on the mobility of rubrene single-crystal field-effect transistors, *Appl. Phys. Lett.* **85**, 3899 (2004).
- [39] H. S. Tan, N. Mathews, T. Cahyadi, F. R. Zhu, and S. G. Mhaisalkar, The effect of dielectric constant on device mobilities of high-performance, flexible organic field effect transistors, *Appl. Phys. Lett.* **94**, 263303 (2009).
- [40] J. Veres, S. D. Ogier, S. W. Leeming, D. C. Cupertino, and S. M. Khaffaf, Low- $k$  insulators as the choice of dielectrics in organic field-effect transistors, *Adv. Funct. Mater.* **13**, 199 (2003).
- [41] R. Bansevicius and J. A. Virbalis, Distribution of electric field in the round hole of plane capacitor, *J. Electrostat.* **64**, 226 (2006).